Editors' Suggestion

Characterization of $^{171}Yb^{3+}$:YVO_4 for photonic quantum technologies

Jonathan M. Kindem,[1,2] John G. Bartholomew,[1,2] Philip J. T. Woodburn,[3] Tian Zhong,[1,2,4] Ioana Craiciu,[1,2] Rufus L. Cone,[3] Charles W. Thiel,[3] and Andrei Faraon[1,2,*]

[1]*Kavli Nanoscience Institute and Thomas J. Watson, Sr., Laboratory of Applied Physics, California Institute of Technology, Pasadena, California 91125, USA*

[2]*Institute for Quantum Information and Matter, California Institute of Technology, Pasadena, California 91125, USA*

[3]*Department of Physics, Montana State University, Bozeman, Montana 59717, USA*

[4]*Institute of Molecular Engineering, University of Chicago, Chicago, Illinois 60637, USA*

(Received 2 May 2018; published 5 July 2018)

Rare-earth ions in crystals are a proven solid-state platform for quantum technologies in the ensemble regime and attractive for new opportunities at the single-ion level. Among the trivalent rare earths, $^{171}Yb^{3+}$ is unique in that it possesses a single $4f$ excited-state manifold and is the only paramagnetic isotope with a nuclear spin of $1/2$. In this work, we present measurements of the optical and spin properties of $^{171}Yb^{3+}$:YVO_4 to assess whether this distinct energy-level structure can be harnessed for quantum interfaces. The material was found to possess large optical absorption compared to other rare-earth-doped crystals owing to the combination of narrow inhomogeneous broadening and a large transition oscillator strength. In moderate magnetic fields, we measure optical linewidths less than 3 kHz and nuclear spin linewidths less than 50 Hz. We characterize the excited-state hyperfine and Zeeman interactions in this system, which enables the engineering of a Λ system and demonstration of all-optical coherent control over the nuclear-spin ensemble. Given these properties, $^{171}Yb^{3+}$:YVO_4 has significant potential for building quantum interfaces such as ensemble-based memories, microwave-to-optical transducers, and optically addressable single rare-earth-ion spin qubits.

DOI: 10.1103/PhysRevB.98.024404

I. INTRODUCTION

Future quantum networks will incorporate a number of different quantum technologies, such as stationary qubits for high-fidelity logic operations and quantum memories for synchronization and long-term storage [1–3]. A successful network will require robust interfaces to coherently map quantum information between the best technologies, which may be based on disparate physical systems. For example, quantum transducers between the microwave and optical domains could be used to interface superconducting processors over long distances through optical networks [4].

Rare-earth ions (REIs) doped into crystalline hosts have demonstrated significant progress in implementing solid-state quantum technologies. REIs possess some of the longest optical and spin coherence lifetimes in the solid state [5–8], which has provided the foundation for numerous demonstrations of quantum memories and quantum interfaces [9–14]. For interfaces involving both microwave and optical photons, REIs with an odd number of electrons (i.e., Kramers ions), such as erbium, neodymium, and ytterbium, are of interest due to their electron-spin transitions. The large magnetic moments of these ions allow for strong interactions with microwaves, enabling fast operations and the potential for interfacing with superconducting qubits. Isotopes of these ions with nonzero nuclear spin also offer the possibility of long-term quantum storage [8]. This combination of properties creates the potential for building interfaces between microwave photons, optical photons, and long-lived nuclear spins.

Among the Kramers ions, ytterbium is an attractive choice due to its simple level structure consisting of only two electronic multiplets. The optical transition between the lowest energy levels of these multiplets occurs around 980 nm, which is readily accessible by standard diode lasers. Furthermore, the $^{171}Yb^{3+}$ isotope is unique among the trivalent REIs as the only Kramers ion with a nuclear spin of $1/2$. This gives the simplest possible hyperfine energy structure allowing for both electron- and nuclear-spin degrees of freedom, reducing the complexity of optical preparation and manipulation of spin states [15,16]. Recent work in $^{171}Yb^{3+}$:Y_2SiO_5 [17–20], Yb^{3+}:$LiNbO_3$ [21], and Yb^{3+}:YAG [22] highlights the interest in this ion. In this work, we investigate $^{171}Yb^{3+}$ doped into the host crystal YVO_4. YVO_4 is an attractive choice for implementing quantum interfaces [23,24] due to the ability to fabricate nanoscale devices [25] and high site symmetry in this material. Furthermore, previous work points to the potential for high oscillator strength transitions for Yb^{3+} doped into YVO_4 [26].

We present an initial survey of the properties of optical and nuclear-spin transitions in $^{171}Yb^{3+}$:YVO_4 at cryogenic temperatures. To determine whether this material can be used for efficient interactions with light, we characterized the strength and inhomogeneity of the optical transitions using high-resolution optical spectroscopy. Large hyperfine couplings and narrow optical inhomogeneous lines in this material result in resolved optical transitions between the hyperfine states, which allowed for characterization of the excited-state

*faraon@caltech.edu

spin Hamiltonian directly from absorption measurements in an applied magnetic field. Knowledge of the spin Hamiltonian enables the identification of magnetic-field orientations that create strongly spin-conserving transitions (for cyclic transitions) or strongly spin-mixing optical transitions (allowing for efficient lambda systems). To assess the possibility of storage and manipulation of quantum information in this material, we measured the coherence properties of the optical and nuclear-spin transitions as a function of applied magnetic field. To demonstrate the potential for all-optical control of the nuclear spin states, we also measured spin echoes using bichromatic Raman pulses.

This paper is organized as follows: Section II presents the material properties of the samples used in this work and the spin Hamiltonian used to model this system. Section III describes the experimental methods and apparatus. Section IV presents the experimental results and discussion. This section is further divided into subsections: A (optical-absorption spectroscopy), B (optical transition strengths), C (excited-state lifetime), D (optical coherence measurements), E (nuclear-spin measurements), and F (all-optical spin coherence measurements).

II. BACKGROUND

A. Material properties

YVO_4 (also called yttrium orthovanadate or YVO) forms a zircon tetragonal crystal with D_{4h} symmetry [27]. Ytterbium substitutes for yttrium in sites of local D_{2d} point-group symmetry. The z axis of the site coincides with the crystalline fourfold axis (the c axis of the crystal). The uniaxial nature of this site reduces the number of parameters needed to characterize the system compared to a lower symmetry crystal such as Y_2SiO_5 [17,18].

The majority of measurements presented in this paper were performed in samples cut from a boule of YVO_4 doped with isotopically enriched $^{171}Yb^{3+}$ custom grown by Gamdan Optics. The concentration of ^{171}Yb was measured to be 100 ppm using secondary ion mass spectrometry (SIMS). The samples were cut and polished to various thicknesses appropriate to each measurement. Fluorescence lifetime measurements were performed using a nominally undoped sample of YVO_4 (Gamdan Optics), which was measured using SIMS to have a residual $^{171}Yb^{3+}$ concentration of approximately 2 ppm.

B. Spin Hamiltonian

The $4f^{13}$ configuration of Yb^{3+} consists of two electronic multiplets: $^2F_{7/2}$ and $^2F_{5/2}$. In the crystal field of YVO_4, the ground-state multiplet ($^2F_{7/2}$) splits into four Kramers doublets and the excited-state multiplet ($^2F_{5/2}$) splits into three Kramers doublets. The energies of these crystal-field levels have been measured previously [28] and are shown in Fig. 1(a). At liquid-helium temperatures, only the lowest energy doublet of the ground state is thermally occupied. The optical transition of interest for quantum interfaces is between the lowest energy doublets of the ground state and excited state [$^2F_{7/2}(0) \rightarrow {}^2F_{5/2}(0)$]. This transition occurs at approximately 984.5 nm for Yb^{3+} doped into YVO_4.

In this work, we focus on the ^{171}Yb isotope, which has a nuclear spin $I = 1/2$. Treating the Kramers doublets as effective spins with $S = 1/2$, we can describe the system with the following spin Hamiltonian [29]:

$$H_{\text{eff}} = \mu_B \mathbf{B}\cdot\mathbf{g}\cdot\mathbf{S} + \mathbf{I}\cdot\mathbf{A}\cdot\mathbf{S} - \mu_n \mathbf{B}\cdot\mathbf{g_n}\cdot\mathbf{I}. \quad (1)$$

The first term is due to the electronic Zeeman interaction, where μ_B is the Bohr magneton, $\mathbf{B}$ is the applied magnetic field, $\mathbf{g}$ is the electronic Zeeman tensor, and $\mathbf{S}$ is the spin-1/2 operator. The second term describes the coupling between the electron spin and nuclear spin via the hyperfine interaction, where $\mathbf{I}$ is the nuclear-spin operator and $\mathbf{A}$ is the hyperfine interaction tensor. The last term arises from the nuclear Zeeman interaction, where μ_n is the nuclear magneton and $\mathbf{g_n}$ is the nuclear Zeeman tensor. For ^{171}Yb in YVO_4, the nonzero components of $\mathbf{g_n}$ will be of the order of the gyromagnetic moment of the free nucleus $g_n = 0.987$, which leads to a nuclear Zeeman interaction ~2000 times smaller than the electronic Zeeman term. For the magnetic-field values used in this work, we treat this interaction by incorporating it into the electronic Zeeman tensor.

The energy structure in the absence of an external magnetic field ($\mathbf{B} = 0$) is determined by the hyperfine interaction $\mathbf{I}\cdot\mathbf{A}\cdot\mathbf{S}$. In the site symmetry of YVO_4, the degeneracy of these levels is partially lifted and the Hamiltonian has the following eigenvalues at zero field: $E = \frac{A_\parallel}{4}, \frac{A_\parallel}{4}, \frac{-A_\parallel+2A_\perp}{4}, \frac{-A_\parallel-2A_\perp}{4}$, where $A_\perp$ and $A_\parallel$ are the components of the hyperfine tensor $\mathbf{A}$ perpendicular and parallel to the crystal symmetry axis (the c axis) [29]. The order of the energies is determined by the signs of these components, which we have determined to be $A_\parallel^g < 0$ and $A_\perp^g, A_\parallel^e, A_\perp^e > 0$ (see Sec. IV A) with the superscript g (e) denoting the ground (excited) state. The corresponding eigenstates numbered from lowest to highest energy are

$$|1\rangle_g = |{\uparrow}\Uparrow\rangle_g, \qquad |1\rangle_e = \frac{1}{\sqrt{2}}(|{\uparrow}\Downarrow\rangle_e - |{\downarrow}\Uparrow\rangle_e), \quad (2)$$

$$|2\rangle_g = |{\downarrow}\Downarrow\rangle_g, \qquad |2\rangle_e = \frac{1}{\sqrt{2}}(|{\uparrow}\Downarrow\rangle_e + |{\downarrow}\Uparrow\rangle_e), \quad (3)$$

$$|3\rangle_g = \frac{1}{\sqrt{2}}(|{\uparrow}\Downarrow\rangle_g - |{\downarrow}\Uparrow\rangle_g), \qquad |3\rangle_e = |{\uparrow}\Uparrow\rangle_e, \quad (4)$$

$$|4\rangle_g = \frac{1}{\sqrt{2}}(|{\uparrow}\Downarrow\rangle_g + |{\downarrow}\Uparrow\rangle_g), \qquad |4\rangle_e = |{\downarrow}\Downarrow\rangle_e. \quad (5)$$

We denote the electron-spin components as $|{\uparrow}\rangle \equiv |S_z = \frac{1}{2}\rangle$, $|{\downarrow}\rangle \equiv |S_z = -\frac{1}{2}\rangle$ and the nuclear-spin components as $|\Uparrow\rangle \equiv |I_z = \frac{1}{2}\rangle$, $|\Downarrow\rangle \equiv |I_z = -\frac{1}{2}\rangle$.

For high magnetic fields applied along the c axis, the electronic Zeeman interaction dominates over the hyperfine interaction. In this regime, mixing between the electron and nuclear spin is greatly reduced and the states effectively become

$$|1'\rangle_g \approx |{\uparrow}\Uparrow\rangle, \qquad |1'\rangle_e \approx |{\downarrow}\Uparrow\rangle, \quad (6)$$

$$|2'\rangle_g \approx |{\uparrow}\Downarrow\rangle, \qquad |2'\rangle_e \approx |{\downarrow}\Downarrow\rangle, \quad (7)$$

$$|3'\rangle_g \approx |{\downarrow}\Downarrow\rangle, \qquad |3'\rangle_e \approx |{\uparrow}\Downarrow\rangle, \quad (8)$$

$$|4'\rangle_g \approx |{\downarrow}\Uparrow\rangle, \qquad |4'\rangle_e \approx |{\uparrow}\Uparrow\rangle. \quad (9)$$

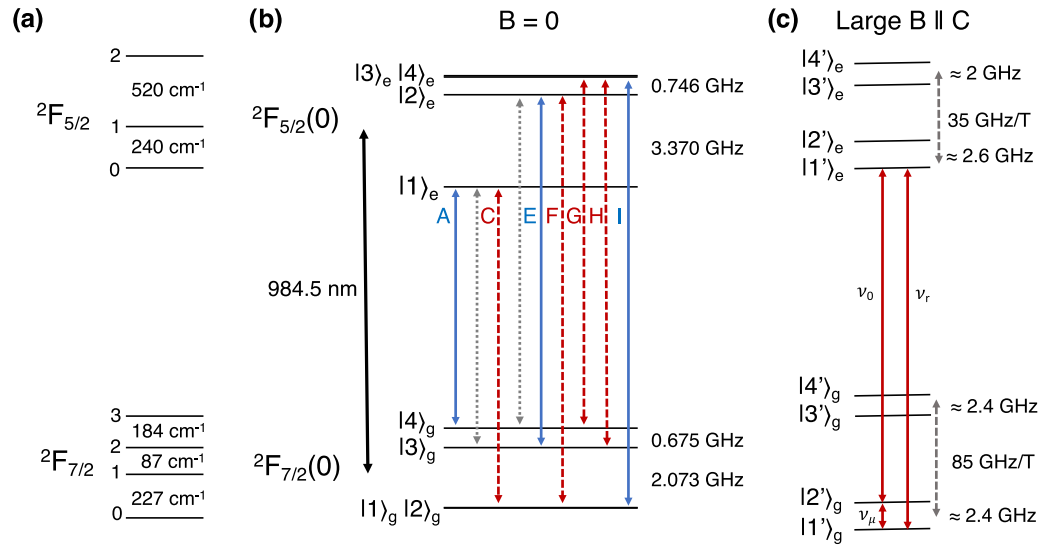

FIG. 1. Energy-level diagram for $^{171}Yb^{3+}$:YVO_4. (a) Crystal-field splittings of $^{171}Yb^{3+}$:YVO_4 reproduced from [28]. (b) Zero-field energy-level diagram for the ${}^2F_{7/2}(0) \rightarrow {}^2F_{5/2}(0)$ transition of $^{171}Yb^{3+}$:YVO_4 at 984.5 nm studied in this paper. Energy splittings in the ground and excited state are extracted from the excited-state hyperfine tensor determined in this work and previous measurements of the ground-state hyperfine tensor [30]. The transitions corresponding to the observed absorption spectrum in Fig. 2 for $E \parallel c$ ($E \perp c$) are shown in solid blue (dashed red). The dotted grey lines correspond to transitions that are forbidden by symmetry. (c) Energy-level diagram for the linear Zeeman regime with $B \parallel c$ with arrows denoting the transitions studied in this work.

We have again numbered the states from lowest to highest energy using the fact that $g_\parallel < 0$ for the ground state and $g_\parallel > 0$ for the excited state (see Sec. IV A). The prime is used to distinguish between the high-field and zero-field state labels. In this work, we focus on the coherence properties of the optical and nuclear-spin transitions in the regime where the linear Zeeman interaction is dominant.

III. EXPERIMENTAL METHODS

High-resolution laser absorption scans with a home-built external-cavity diode laser (ECDL) using the design from [31] were performed to measure the inhomogeneous linewidth and absorption of the ${}^2F_{7/2}(0) \rightarrow {}^2F_{5/2}(0)$ transition. The energies of the optical transitions were extracted from absorption scans taken with magnetic fields applied along the crystal symmetry axes and used to determine the excited-state spin Hamiltonian. For this purpose, we used a 90-μm-thick a-cut sample of $^{171}Yb^{3+}$:YVO_4. This thickness was chosen such that the sample was not overabsorbing at 2 K. The sample was mounted in a custom sample mount and masked to avoid spurious light leakage around the crystal that could lead to inaccurate measurements of the optical depth. For the data presented here, the probe light propagated parallel to the a axis of the crystal and perpendicular to the applied magnetic field ($\mathbf{k} \perp \mathbf{B}, c$). Additional axial spectra ($\mathbf{k} \parallel c$) were taken to confirm the electric dipole nature of the optical transitions [32]. The absorption was determined by measuring the transmission of the ECDL on a photodetector (New Focus 2031) as the frequency of the laser was scanned across resonance. The center frequency of the scan was calibrated with a wave meter (Burleigh WA-1500) and the frequency detuning of the scan was calibrated using a Fabry-Perot reference cavity. The absorption experiments were performed in an Oxford Spectromag cryostat at a temperature of 2 K with an applied magnetic field of up to 6 T.

For measurements of the excited state, optical coherence, and spin coherence lifetimes, the optical transitions were addressed using a single frequency Ti:sapphire laser (M-Squared Solstis) that was gated by an 80-MHz acousto-optic modulator in a double-pass configuration to create the required pulse sequence. For measurements of the coherence properties and inhomogeneity of the nuclear-spin transition, the nuclear-spin transition was addressed directly using a coaxial transmission line mounted directly next to the sample.

The excited-state lifetime was measured from the time-resolved fluorescence decay. We performed pulsed excitation on the ${}^2F_{7/2}(0) \rightarrow {}^2F_{5/2}(0)$ transition and collected the resulting fluorescence to the upper crystal-field levels of the ground state [i.e., ${}^2F_{5/2}(0) \rightarrow {}^2F_{7/2}(1-3)$] using a 1000-nm long-pass filter. The fluorescence counts as a function of time were recorded using a silicon avalanche photodiode (Perkin-Elmer). Fluorescence measurements were performed in a 500-μm-thick sample that was nominally undoped (residual $^{171}Yb^{3+}$ concentration of $\sim$2 ppm) and a 200-μm-thick 100-ppm sample of $^{171}Yb^{3+}$:YVO_4. These measurements were performed at 4 K with zero applied magnetic field in a Montana Instruments cryostat using a home-built confocal microscope setup.

The coherence properties of the optical transition were investigated using two-pulse photon echo decays as a function of magnetic field strength. For this purpose, two-pulse photon echoes on the $|1'\rangle_g \rightarrow |1'\rangle_e$ transition were measured using heterodyne detection. During the echo sequence, a fiber-based phase modulator EOM (IXBlue NIR-MPX-LN-20) was driven by a microwave source (Windfreak Synth HD) at 500 MHz to create an optical sideband resonant with the optical transition. The resulting echo was detected as a beat at the sideband

frequency using an InGaAs photodiode (Thorlabs DET08CFC, 5 GHz bandwidth). Typical π pulses for this measurement were 4 μs long.

Optical coherence measurements were performed with the sample mounted on the still plate of a Bluefors dilution refrigerator at a temperature of 650 mK. These measurements used a 500-μm-thick c-cut 100-ppm sample with $\mathbf{k} \parallel c$. The light entered the refrigerator via single-mode optical fiber and was focused onto the back surface of the sample, which was coated in gold to enhance reflection. The reflected light was coupled back into the fiber and directed to the photodetector with a fiber beam splitter. A variable magnetic field of up to 1.5 T was applied along the crystal c axis using a home-built superconducting solenoid.

The inhomogeneous linewidth of the nuclear-spin transition was measured using continuous-wave Raman heterodyne detection [33]. Frequency-swept microwave tones from a tracking generator (Anritsu) were amplified and applied to the sample. The coherence generated on the $|1'\rangle_g \rightarrow |2'\rangle_g$ nuclear-spin transition was mapped to an optical coherence by applying a continuous-wave laser to the $|2'\rangle_g \rightarrow |1'\rangle_e$ optical transition at frequency ν_0, which resulted in coherent Raman scattering on the $|1'\rangle_g \rightarrow |1'\rangle_e$ optical transition at ν_r. This signal was detected on the transmitted optical beam as a beat at the microwave transition frequency $(\nu_0 - \nu_r)$ using an InGaAs photodiode.

The nuclear-spin coherence was measured using two-pulse spin echoes. Coherent manipulation on the nuclear-spin state was performed with both direct microwave excitation and all-optical excitation with bichromatic Raman pulses [34–37]. The ions were first initialized into the $|1'\rangle_g$ state via optical pumping on the $|2'\rangle_g \rightarrow |1'\rangle_e$ transition. For direct manipulation, the echo sequence was performed using tones generated by a microwave source tuned to the $|1'\rangle_g \rightarrow |2'\rangle_g$ nuclear spin transition. Pulses were generated using microwave switches (Minicircuits ZASWA-2-50DR+) with typical π pulse lengths of 100 μs. For all-optical spin echoes, the nuclear-spin transition was coherently manipulated via the shared excited state $|1'\rangle_e$ by applying bichromatic pulses to the $|2'\rangle_g \rightarrow |1'\rangle_e$ and $|1'\rangle_g \rightarrow |1'\rangle_e$ transitions as depicted in Fig. 1(c). Typical spin π pulses for the all-optical sequence were 8 μs. The two optical frequencies were generated by driving a fiber-based phase modulator with a microwave source tuned to the nuclear-spin transition frequency. The relative power of the two optical frequencies was chosen to maximize the echo signal. The resulting spin echo was optically detected via Raman heterodyne scattering by applying a readout pulse to the $|2'\rangle_g \rightarrow |1'\rangle_e$ transition at the time of the echo. The signal was detected as a beat on the probe laser at the nuclear-spin transition frequency.

Nuclear-spin coherence measurements were performed at approximately 700 mK. These measurements were done in transmission through a 2-mm-thick a-cut sample with $\mathbf{k} \perp c, \mathbf{B}$. The polarization of the input light was set using a fiber polarization controller to maximize the echo signal. A variable magnetic field was applied to the crystal using a set of home-built superconducting Helmholtz coils. For the direct microwave measurements, the magnetic field was applied along the c axis. For the all-optical measurements, the magnetic field was applied $\sim 20^\circ$ from the c axis. As described in Sec. IV, this was done to help equalize the strengths of the optical transitions used in the measurement.

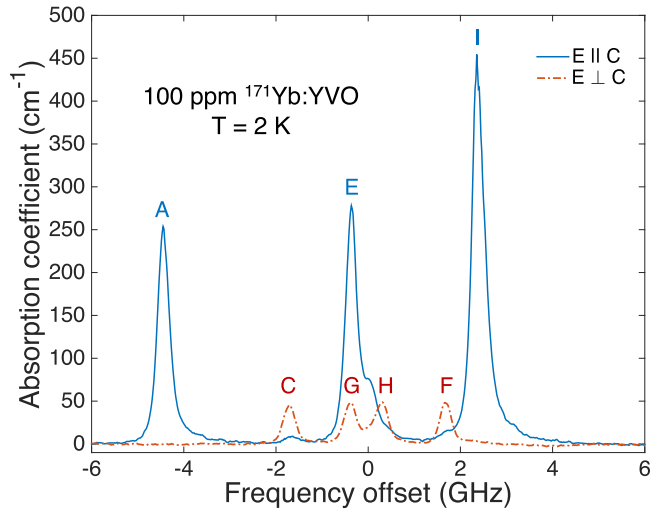

FIG. 2. Optical-absorption spectra of the $^2F_{7/2}(0) \rightarrow {}^2F_{5/2}(0)$ transition of $^{171}Yb^{3+}$:YVO_4 at 2 K and zero applied magnetic field for light polarized parallel (solid blue) and perpendicular (dashed red) to the crystal c axis.

IV. OPTICAL AND SPIN PROPERTIES OF ^{171}Yb:YVO_4

A. Optical-absorption spectroscopy

The zero-field absorption spectra for the $^2F_{7/2}(0) \rightarrow {}^2F_{5/2}(0)$ transition of $^{171}Yb^{3+}$:YVO_4 at 2 K is shown in Fig. 2. We observed narrow inhomogeneous linewidths [the average full width at half maximum (FWHM) is 275 MHz], which allowed us to resolve and address individual optical-hyperfine transitions. For $\mathbf{E} \parallel c$, we observed three resolved transitions with a peak absorption coefficient for the strongest transition of 450 cm^{-1}. For $\mathbf{E} \perp c$, we observed four resolved transitions with a peak absorption of 50 cm^{-1}. The corresponding transitions on the energy diagram are labeled in Fig. 1(b). The strong polarization selection rules between the optical hyperfine transitions observed in Fig. 2 are consistent with those derived for electric-dipole transitions based on the site's point-group symmetry [38].

We observed a peak at zero detuning, which corresponds to the presence of zero-spin isotope in the sample (measured to be $<$10 ppm from SIMS). We also noted the presence of additional satellite lines due to the 173 isotope.

The ground-state Zeeman and hyperfine tensors of $^{171}Yb^{3+}$:YVO_4 have been determined using electron paramagnetic resonance [30], so a description of the system requires finding the corresponding values for the excited state. For a uniaxial crystal, this reduces to four parameters: the components of $\mathbf{g}$ and $\mathbf{A}$, parallel and perpendicular to the crystal symmetry axis. The values for $\mathbf{A}$ can be determined by the energy-level structure in the absence of a magnetic field, while $\mathbf{g}$ can be determined from the energy-level structure as magnetic fields are applied parallel and perpendicular to the crystal's c axis.

Fitting to the energy-level splittings extracted from the absorption spectra, we find agreement with previously published

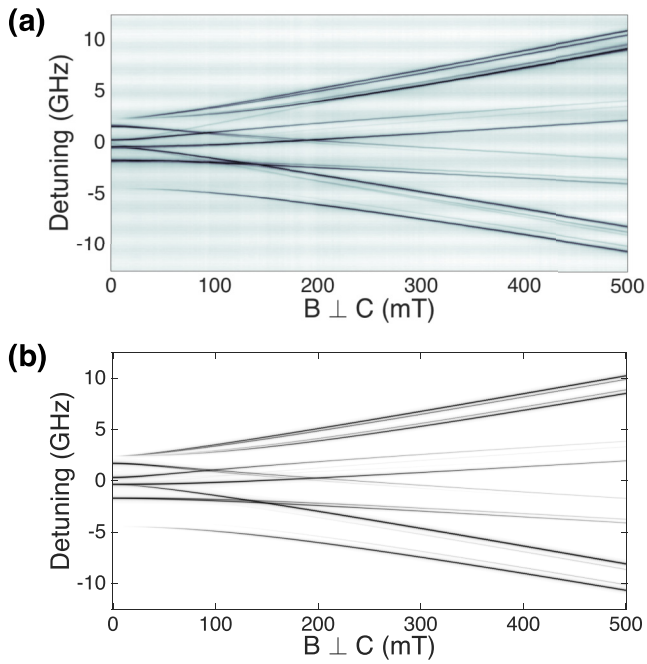

FIG. 3. (a) Typical high-resolution absorption spectra for a magnetic field ramp with B,$\mathbf{k} \perp c$ and $\mathbf{E} \perp c$ showing resolved optical hyperfine transitions. Darker regions correspond to higher absorption. (b) Simulated absorption spectra using the experimentally determined spin Hamiltonian for magnetic field ramp with B,$\mathbf{k} \perp c$ and $\mathbf{E} \perp c$. The simulated absorption spectra take into account a slight misalignment ($\sim 1^\circ$) between the crystal a axis and the applied magnetic field.

data for the ground-state **A** tensor [30] ($A^g_\parallel/h = -4.82$ GHz, $A^g_\perp/h = 0.675$ GHz) and we determine the principal values of the excited-state hyperfine tensor to be $A^e_\parallel/h = 4.86 \pm 0.05$ GHz and $A^e_\perp/h = 3.37 \pm 0.05$ GHz.

The excited-state **g** tensor was determined by measuring the frequency of the optical transitions with magnetic fields applied parallel and perpendicular to the crystal's c axis. Figure 3(a) shows an example of one such measurement in which the absorption was recorded while the magnetic field perpendicular to the crystal c axis was continuously ramped. By fitting to the energy levels extracted from this spectra and similar measurements for other field orientations, we determine $g_{e,\parallel} = 2.51 \pm 0.1$ and $g_{e,\perp} = 1.7 \pm 0.1$. Figure 3(b) shows the absorption spectra expected from the spin Hamiltonian, which we see enables accurate predictions of the energy-level splittings and relative transition absorption oscillator strengths in this case.

B. Optical transition strengths

The strength of the optical transitions can be characterized by assigning an oscillator strength to each individual transition. The absorption oscillator strength for a transition $|i\rangle \rightarrow |j\rangle$ for a polarized spectrum is given by [39,40]

$$f_{ij} = 4\pi\epsilon_0 \frac{m_e c}{\pi e^2} \frac{1}{N} \sum_i \frac{9n_i}{\left(n_i^2+2\right)^2} \int \alpha_i(\nu) d\nu, \qquad (10)$$

where ϵ_0 is the vacuum permittivity, m_e is the mass of the electron, e is the charge on the electron, c is the speed of light, N is the number density, and the summation is over the three orthogonal polarizations states with α_i and n_i absorption coefficient and index of refraction, respectively. For YVO_4, $n_\parallel = 2.17$ and $n_\perp = 1.96$ at 984 nm [41].

TABLE I. Absorption properties of the $^{171}Yb^{3+}$:YVO_4 transitions as labeled in Fig. 2, including the transition polarization [38], integrated absorption coefficient, oscillator strength, and radiative decay rate at zero magnetic field.

Trans.	Pol.	$\int \alpha(\nu) d\nu$ (GHz/cm)	f (10^{-6})	$1/\tau_{rad}$ (kHz)
A	π	97.3	5.4	1.3
C	σ	16.4	1.0	0.3
E	π	102.7	5.5	1.4
F	σ	17.4	1.1	0.4
G	σ	20.2	2.6	0.2
H	σ	19.9	2.6	0.2
I	π	189.7	4.9	1.2

Assuming a doping density of 100 ppm, the number density of Yb^{3+} in YVO_4 is calculated to be $N = 1.24 \times 10^{18}$ cm^{-3}, which is distributed between the four ground-state levels according to Boltzmann statistics at 2 K. The integrated absorption coefficient and corresponding oscillator strengths for the observed transitions are summarized in Table I. We measure an average oscillator strength of 5.3×10^{-6} for transitions allowed for $\mathbf{E} \parallel c$ (transitions A, E, I in Fig. 2) and 1.8×10^{-6} for transitions allowed for $\mathbf{E} \perp c$ (transitions C, F, G, H in Fig. 2).

The radiative lifetime for the $^2F_{5/2}(0) \rightarrow {}^2F_{7/2}(0)$ transitions can be determined from the absorption measurements. The radiative lifetime for a transition $|j\rangle \rightarrow |i\rangle$ is related to the oscillator strength by [39,40]

$$\frac{1}{\tau_{rad}} = \frac{2\pi e^2}{\epsilon_0 m_e c} \frac{(n^2+2)^2}{9n} \frac{n^2}{\lambda_0^2} \frac{f_{ji}}{3}, \qquad (11)$$

where n is the index of refraction, λ_0 is the wavelength in vacuum, and f_{ji} is the emission oscillator strength. The emission oscillator strength is related to the absorption oscillator strength f_{ij} by $f_{ji} = \frac{g_i}{g_j} f_{ij}$, where g_i (g_j) is the degeneracy of state $|i\rangle$ ($|j\rangle$). The calculated emission rates for the observed transitions are included in Table I. From these rates, we obtain an average radiative rate of $1/\tau_{rad} = 1/(590\ \mu s)$ for the $^2F_{5/2}(0) \rightarrow {}^2F_{7/2}(0)$ transitions.

C. Excited-state lifetimes

The excited-state lifetime is important for optical preparation of population among the spin states and sets the upper limit on the optical coherence time. The measured excited-state lifetime allow us to determine the optical branching ratio between the crystal-field levels, which is important in the context of Purcell enhancement in nanophotonic cavities [42]. Here, we measure the excited-state lifetime through fluorescence decay.

To avoid the problem of radiation trapping [43] observed in previous measurements of excited-state lifetimes in Yb-doped materials [22,26,44], the excited-state lifetime was measured in a nominally undoped sample of YVO_4, which had

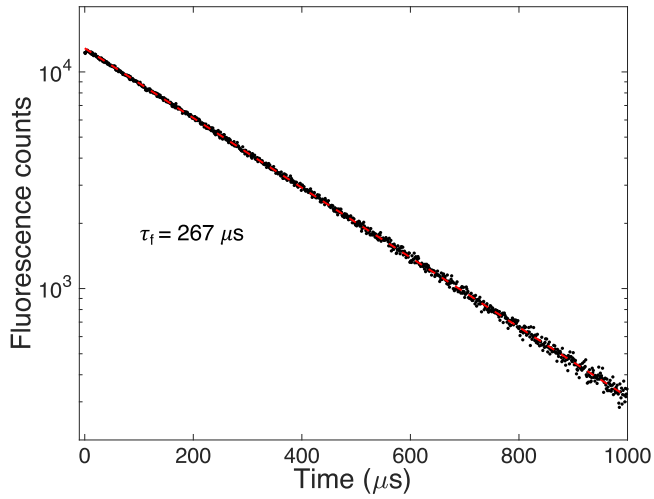

FIG. 4. Excited-state lifetime measurement via fluorescence decay. An exponential fit (dashed line) gives $\tau_f = 267 \pm 1\ \mu$s.

a residual $^{171}Yb^{3+}$ concentration of approximately 2 ppm. In this sample, we did not see variations in the optical lifetime within the inhomogeneous line or other signs of radiation trapping. A typical fluorescence decay in this sample is shown in Fig. 4. Fitting to a single exponential gives a fluorescence lifetime of $\tau_f = 267 \pm 1\ \mu$s. The branching ratio back to the same crystal-field level $[^2F_{5/2}(0) \rightarrow {}^2F_{7/2}(0)]$ is then given by $\beta = \tau_f/\tau_{\text{rad}}$, where τ_f and τ_{rad} are the fluorescence and radiative lifetimes. Using the radiative lifetime obtained from the absorption measurements, we determine the branching ratio to be $\beta = 0.45$.

We also note that in a 200-μm-thick 100-ppm sample we observed lifetimes longer than 500 μs in the center of the inhomogeneous distribution that decreased to less than 300 μs when the excitation pulse was detuned by 200 MHz from the center of the line. This behavior is attributed to radiation trapping due to the high optical depth and strong transition strengths of these ions.

D. Optical coherence measurements

To assess the ability to store quantum states in the material, we first investigate the coherence of the optical transition using two-pulse photon echoes (2PPEs). For Kramers ions, we expect a dominant source of decoherence to be magnetic fluctuations due to magnetic dipole-dipole interactions between Yb ions [45]. One way to minimize this source of decoherence is to freeze-out the electron spins by achieving a ground-state splitting much larger than k_bT [45]. For $^{171}Yb^{3+}$:YVO_4, the energy-level splitting is maximized for a magnetic field along the crystal c axis. Here, we present measurements of the optical coherence in the linear Zeeman regime with the magnetic field along the c axis. While a comprehensive study is warranted to fully understand the decoherence mechanisms in this system, a large magnetic field applied parallel to c provides insight on the maximum achievable coherence times in this material and the dominant decoherence mechanisms.

Figure 5(a) shows typical photon echo decays for magnetic fields ranging from 340 mT to 1.36 T along the crystal c axis. We observed strong nonexponential decays, which can be attributed to spectral diffusion and described by a Mims decay [46]. For heterodyne detection, the decay of the echo field is given by [46]

$$E(t_{12}) = E_0 e^{-(2t_{12}/T_m)^x}, \tag{12}$$

where t_{12} is the delay between the two pulses used in the photon echo experiment, x is the Mims parameter describing the spectral diffusion, and T_m is phase memory time (the time at which the echo field amplitude decays to e^{-1} of its initial value). Fits to the Mims decay are shown as solid lines in Fig. 5(a). From T_m, we can extract an effective homogeneous linewidth as $\Gamma_{\text{h,eff}} = (\pi T_m)^{-1}$. The effective linewidth as a function of applied magnetic field along the c axis is shown in Fig. 5(b).

We observed a decrease in the linewidth with applied magnetic field from ~5.5 kHz at 340 mT to ~3 kHz at 1.5 T, which was the maximum magnetic field achievable for this measurement. The reduction in linewidth for increasing magnetic field is expected for dephasing dominated by Yb-Yb spin flips and similar to that observed in other Kramers ions [45,47]. At the highest magnetic fields, we saw that the coherence no longer increased with applied field. The nonexponential decay and saturation of coherence time in the high-field limit are typical signs of the superhyperfine limit [48]. In this limit, magnetic fluctuations due to the electron spins are effectively frozen out and the main contribution to dephasing is interactions with the nuclei of the host material.

We note that recent work in $^{171}Yb^{3+}$:Y_2SiO_5 [20] and $^{167}Er^{3+}$:Y_2SiO_5 [49] demonstrated an increase in coherence time due to reduced sensitivity to magnetic fluctuations at zero first-order Zeeman (ZEFOZ) points at $\mathbf{B} = 0$. While we did not explore the low-field regime in this work, Eq. (1) predicts similar zero-field ZEFOZ transitions in $^{171}Yb^{3+}$:YVO_4 between levels $|3\rangle_g$ and $|4\rangle_g$ of the ground state and $|1\rangle_e$ and $|2\rangle_e$ of the excited state.

E. Nuclear-spin measurements

The coherence times of the $^2F_{7/2}(0)$ nuclear-spin transitions will determine the feasibility of long-term quantum information storage in this system. In this section, we present measurements on the inhomogeneous linewidth and coherence properties of the $|1'\rangle_g \rightarrow |2'\rangle_g$ nuclear-spin transition in the linear Zeeman regime.

The inhomogeneous broadening of the nuclear-spin transition was measured using continuous-wave Raman heterodyne spectroscopy [33]. Figure 6 shows a typical trace of the normalized Raman heterodyne signal power as the microwave frequency is swept across the resonance. Fitting this peak to a Lorentzian gives a FWHM of 250 kHz, which serves as an upper bound on the inhomogeneous broadening of the spin transition since the width of the observed signal can be power broadened by the Rabi frequencies of the optical and microwave fields used in the measurement [50]. The inhomogeneity of the nuclear-spin transition can be attributed to variations in the crystal field due to strain and defects in the crystal and variations in the local magnetic field arising from spin-spin interactions [51], as well as inhomogeneity of the applied magnetic field along the beam path. This measurement

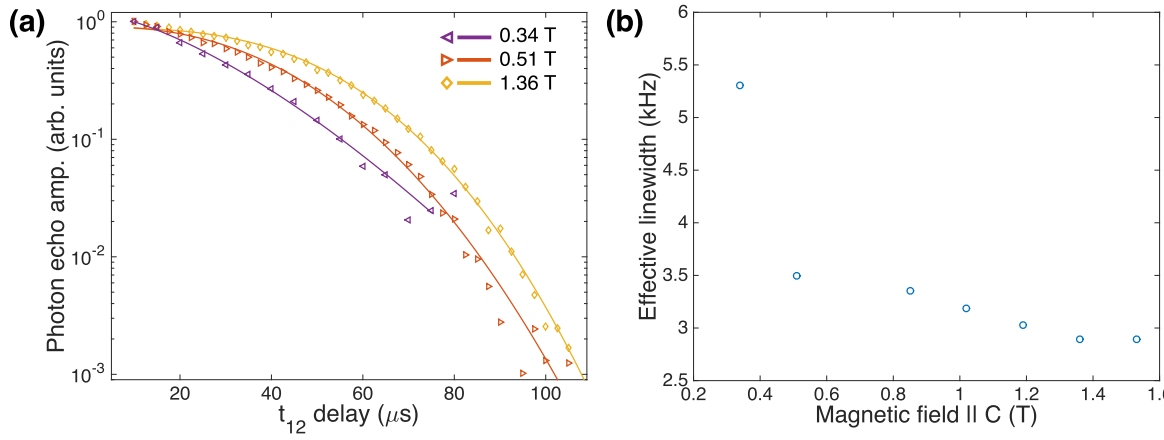

FIG. 5. (a) Typical photon echo decays for $B \parallel c$ showing an increase of coherence time and strong nonexponential decays with increasing magnetic field. Fits to a Mims decay are shown for each field value as a solid line (see main text for details). (b) Effective linewidth extracted from the fits to the photon echo decays for $B \parallel c$.

was done with a field of 440 mT along c, but is typical of what was obtained for other magnetic field amplitudes applied along this direction.

The nuclear-spin coherence was measured by spin-echo decays with direct microwave manipulation of the $|1'\rangle_g \rightarrow |2'\rangle_g$ spin transition and optical detection via coherent Raman scattering. Figure 7 shows typical nuclear-spin echo decays for increasing magnetic fields along the c axis. For the higher field decays, we observed nonexponential decays resulting from time-varying dephasing mechanisms that can again be described by the Mims decay using Eq. (12). We measured coherence times of 250 μs at 60 mT that increased up to 6.6 ms at a field of 440 mT, which was the maximum achievable magnetic field for the experimental configuration at the time of the measurement. Time-resolved measurements of the decay of the area of spectral holes prepared in the inhomogeneous line [51] gave spin-relaxation times longer than 200 ms in this field configuration, indicating that these coherence times are not lifetime limited.

F. All-optical spin coherence measurements

In addition to direct microwave excitation of the nuclear spins, we are interested in performing coherent all-optical control on the nuclear spins. All-optical control allows us to take advantage of relatively strong optical transitions to perform faster manipulations on the spin. This approach also removes the need for a microwave circuit to be incorporated next to the sample, which reduces the complexity of the experimental setup and prevents additional heating of the sample through the microwave excitation. As an initial demonstration of the potential for all-optical control in this system, we use an all-optical Raman echo technique [52] to measure the coherence of the nuclear-spin transition. The $|1'\rangle_g \rightarrow |2'\rangle_g$ transition is addressed by applying bichromatic pulses to the lambda system formed by the $|2'\rangle_g \rightarrow |1'\rangle_e$ and $|1'\rangle_g \rightarrow |1'\rangle_e$ optical transitions. Efficient rephasing of coherence on the spin transition using bichromatic pulses in this fashion requires that the Rabi frequencies of the two transitions of the lambda system are

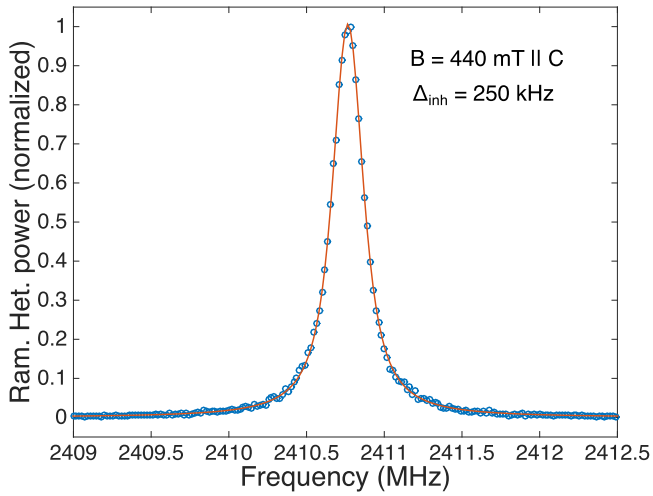

FIG. 6. Continuous-wave Raman heterodyne measurement of the nuclear-spin inhomogeneity with $B = 440$ mT parallel to the c axis. A Lorentzian fit gives a FWHM of 250 kHz.

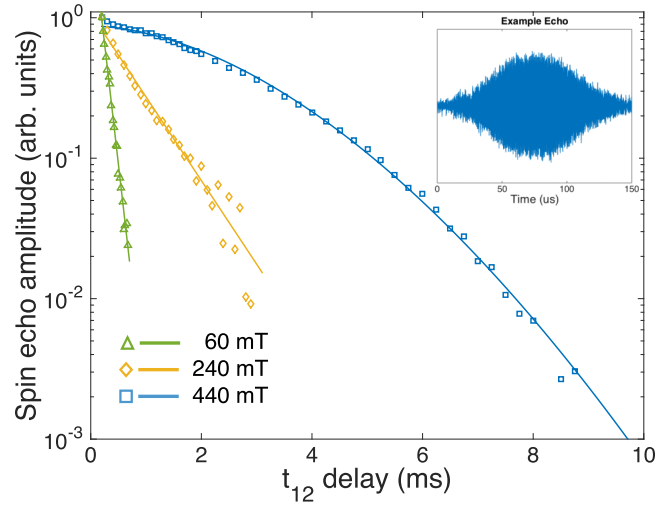

FIG. 7. Typical nuclear-spin echo decays for increasing applied magnetic field along the c axis. The echo sequence is performed with direct microwave excitation and read out optically.

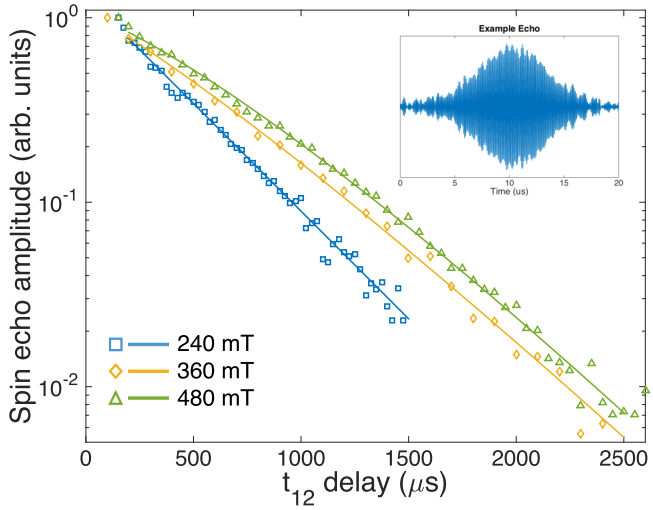

FIG. 8. Typical nuclear-spin-echo decays for increasing magnetic fields applied 20° from the c axis. Here, the entire sequence is performed using all-optical manipulation of the spins.

equal [35]. For magnetic fields applied parallel to the c axis, one transition of the lambda system is weak because the wave functions have approached separability and the optical transition cannot flip the nuclear spin. Moving the field off axis induces mixing of the nuclear and electronic states, which allows for a more favorable branching ratio between the two arms of the lambda system.

Figure 8 shows representative all-optical Raman echo decays for increasing applied magnetic fields applied 20° from the c axis. Fitting to a Mims decay to describe the observed nonexponential behavior gave spin coherence times up to 1 ms at 480 mT, which was the maximum field available for this experiment. We note that moving the field off axis increases the magnetic sensitivity of the transition and therefore we expect a decrease of the spin coherence time in this regime. This configuration also reduces the ground-state splitting, which would increase the contribution from Yb-Yb electron-spin interactions. We expect to extend this coherence time with increasing magnetic fields as observed in the optical coherence measurements.

V. SUMMARY AND CONCLUSION

In this work, we have presented measurements assessing $^{171}Yb^{3+}$:YVO_4 for use in quantum interfaces focusing on the strength of the optical transitions, the energy level structure, and the coherence properties of the optical and spin transitions.

From optical-absorption measurements, we extract oscillator strengths in the upper range of those observed in REIs and larger than those observed for $^{171}Yb^{3+}$ doped into Y_2SiO_5 and YAG [17,22]. This oscillator strength is promising for detecting and manipulating single ions coupled to nanophotonic cavities. The combination of large oscillator strengths and narrow inhomogeneous broadening in this material gives rise to exceptionally large absorption coefficients for this material. Significantly, the peak absorption of 450 cm^{-1} is within a factor of 2 of the absorption in recently studied stoichiometric rare-earth crystals [53], even though the ion concentration is a factor of 10^4 more dilute. This absorption coefficient is promising for ensemble-based memories in bulk samples and reaching the impedance-matched regime necessary to achieve high-efficiency nanophotonic quantum memories. We observe a large branching ratio for relaxation directly to the ground state for the $^2F_{5/2}(0) \rightarrow {}^2F_{7/2}(0)$ transition, which is appealing in the context of Purcell enhancement of the emission rate in a nanocavity [24,54].

The large hyperfine couplings and narrow inhomogeneous linewidths give rise to resolved optical-hyperfine transitions. This is useful for addressing and manipulating single transitions and states without additional preparation. The large nuclear-spin transition splittings are also useful in the context of off-resonance memory schemes and high-bandwidth spin-wave storage. We completed a characterization of the energy-level structure by determining the excited-state spin Hamiltonian. The knowledge of the full spin Hamiltonian is essential for designing optimal quantum interfaces because it facilitates the prediction and engineering of lambda systems or highly cyclic transitions. The symmetry of the crystal gives rise to the strong selection rules on the optical transitions. These selection rules are advantageous for engineering cyclic transitions [55], especially in the context of a nanocavity that can preferentially enhance emission along one polarization.

For protocols requiring additional nuclear-spin states, the ^{173}Yb isotope could be of interest because it has a nuclear spin of 5/2. The knowledge of the spin Hamiltonian for the ^{171}Yb isotope allows the spin Hamiltonian for the ^{173}Yb isotope to be approximated by scaling the hyperfine splittings by the ratio of the nuclear magnetic moments of the isotopes [56].

The optical coherence times are already sufficient for use in quantum applications and are promising from the perspective of reaching transform-limited photons in a nanocavity setting. The observed spin coherence properties show potential for use in spin-wave quantum memories and for single rare-earth ion qubits. In the linear Zeeman regime, the optical coherence times are limited by the superhyperfine interaction in the material. While a higher magnetic field regime was not available for the experimental configuration at the time of measurement, we expect the spin coherence times to increase with applied magnetic field as we completely freeze-out the electron-spin contribution. Further extension of the nuclear-spin coherence time is predicted through the use of dynamic decoupling techniques [7]. We note that the doping density used in these measurements (100 ppm) is relatively high compared to many of the materials used for REI quantum technologies. We expect that by going to lower doping density samples we will reduce the contribution from Yb spin-spin interactions and observe longer optical and spin coherence times in the low-field regime. Furthermore, by moving to lower temperatures, we can hope to freeze-out the electron spins at lower magnetic fields. While this work focused on the optical and nuclear-spin coherence properties in the linear Zeeman regime, we calculate that a zero-field ZEFOZ transition exists for one of the ground-state transitions, which is expected to lead to an enhancement of coherence [20,49]. This configuration would also have the advantage of a strong electron-spin transition between the ground states. Future studies are warranted to investigate the spin coherence properties of this material at lower

doping densities, temperatures, and different magnetic field regimes.

In summary, we find that $^{171}Yb^{3+}$:YVO_4 is a promising material for REI-based quantum interfaces, such as ensemble-based quantum memories, microwave-to-optical transduction, and single REIs in nanophotonic cavities.

ACKNOWLEDGMENTS

This work was funded by Office of Naval Research Young Investigator Award No. N00014-16-1-2676, Northrop Grumman, Montana Research, and Economic Development Initiative, and the National Science Foundation under Grants No. PHY-1415628 and No. CHE-1416454. J.G.B. acknowledges the support of the American Australian Association's Northrop Grumman Fellowship. J.M.K. and J.G.B would like to thank R. L. Cone, C. W. Thiel, and P. J. T. Woodburn for their hospitality throughout the trip to Bozeman during which part of this worked was performed. We would also like to acknowledge the expertise of Dr. Y. Guan who was essential support for the SIMS analysis of the samples, and Dr. P. Oyala who assisted with preliminary bulk EPR measurements of this material.

[1] H. J. Kimble, Nature (London) **453**, 1023 (2008).
[2] T. E. Northup and R. Blatt, Nat. Photonics **8**, 356 (2014).
[3] J. L. O'Brien, A. Furusawa, and J. Vučković, Nat. Photonics **3**, 687 (2009).
[4] R. W. Andrews, R. W. Peterson, T. P. Purdy, K. Cicak, R. W. Simmonds, C. A. Regal, and K. W. Lehnert, Nat. Phys. **10**, 321 (2014).
[5] R. W. Equall, Y. Sun, R. L. Cone, and R. M. Macfarlane, Phys. Rev. Lett. **72**, 2179 (1994).
[6] T. Böttger, C. W. Thiel, R. L. Cone, and Y. Sun, Phys. Rev. B **79**, 115104 (2009).
[7] M. Zhong, M. P. Hedges, R. L. Ahlefeldt, J. G. Bartholomew, S. E. Beavan, S. M. Wittig, J. J. Longdell, and M. J. Sellars, Nature (London) **517**, 177 (2015).
[8] M. Rančić, M. P. Hedges, R. L. Ahlefeldt, and M. J. Sellars, Nat. Phys. **14**, 50 (2017).
[9] W. Tittel, M. Afzelius, T. Chaneliére, R. Cone, S. Kröll, S. Moiseev, and M. Sellars, Laser Photonics Rev. **4**, 244 (2009).
[10] M. P. Hedges, J. J. Longdell, Y. Li, and M. J. Sellars, Nature (London) **465**, 1052 (2010).
[11] M. Sabooni, Q. Li, S. Kröll, and L. Rippe, Phys. Rev. Lett. **110**, 133604 (2013).
[12] E. Saglamyurek, N. Sinclair, J. A. Slater, K. Heshami, D. Oblak, and W. Tittel, New J. Phys. **16**, 065019 (2014).
[13] M. Gündogan, P. M. Ledingham, K. Kutluer, M. Mazzera, and H. de Riedmatten, Phys. Rev. Lett. **114**, 230501 (2015).
[14] C. Laplane, P. Jobez, J. Etesse, N. Timoney, N. Gisin, and M. Afzelius, New J. Phys. **18**, 013006 (2016).
[15] B. Lauritzen, S. R. Hastings-Simon, H. de Riedmatten, M. Afzelius, and N. Gisin, Phys. Rev. A **78**, 043402 (2008).
[16] E. Baldit, K. Bencheikh, P. Monnier, S. Briaudeau, J. A. Levenson, V. Crozatier, I. Lorgeré, F. Bretenaker, J. L. Le Gouët, O. Guillot-Noël, and P. Goldner, Phys. Rev. B **81**, 144303 (2010).
[17] S. Welinski, A. Ferrier, M. Afzelius, and P. Goldner, Phys. Rev. B **94**, 155116 (2016).
[18] A. Tiranov, A. Ortu, S. Welinski, A. Ferrier, P. Goldner, N. Gisin, and M. Afzelius, arXiv:1712.08616.
[19] H.-J. Lim, S. Welinski, A. Ferrier, P. Goldner, and J. J. L. Morton, Phys. Rev. B **97**, 064409 (2018).
[20] A. Ortu, A. Tiranov, S. Welinski, F. Fröwis, N. Gisin, A. Ferrier, P. Goldner, and M. Afzelius, arXiv:1712.08615.
[21] Z. Kis, G. Mandula, K. Lengyel, I. Hajdara, L. Kovacs, and M. Imlau, Opt. Mater. **37**, 845 (2014).
[22] T. Böttger, C. W. Thiel, R. L. Cone, Y. Sun, and A. Faraon, Phys. Rev. B **94**, 045134 (2016).
[23] H. de Riedmatten, M. Afzelius, M. U. Staudt, C. Simon, and N. Gisin, Nature (London) **456**, 773 (2008).
[24] T. Zhong, J. M. Kindem, J. G. Bartholomew, J. Rochman, I. Craiciu, E. Miyazono, M. Bettinelli, E. Cavalli, V. Verma, S. W. Nam, F. Marsili, M. D. Shaw, A. D. Beyer, and A. Faraon, Science **357**, 1395 (2017).
[25] T. Zhong, J. Rochman, J. M. Kindem, E. Miyazono, and A. Faraon, Opt. Express **24**, 536 (2016).
[26] C. Kränkel, D. Fagundes-Peters, S. T. Fredrich, J. Johannsen, M. Mond, G. Huber, M. Bernhagen, and R. Uecker, Appl. Phys. B **79**, 543 (2004).
[27] R. Wyckoff, *Crystal Structures*, 2nd ed. (John Wiley & Sons, New York, 1963).
[28] E. V. Pestryakov, V. V. Petrov, V. I. Trunov, A. V. Kirpichnikov, M. A. Merzliakov, A. V. Laptev, and V. N. Matrosov, Proc. SPIE **6054**, 60540I (2006).
[29] A. Abragam and B. Bleaney, *Electron Paramagnetic Resonance of Transition Ions* (Oxford University Press, Oxford, 1970).
[30] U. Ranon, Phys. Lett. A **28**, 228 (1968).
[31] E. C. Cook, P. J. Martin, T. L. Brown-Heft, J. C. Garman, and D. A. Steck, Rev. Sci. Instrum. **83**, 043101 (2012).
[32] *Spectroscopic Properties of Rare Earths in Optical Materials*, Springer Series in Materials Science Vol. 83, edited by G. Liu and B. Jacquier (Springer-Verlag, Berlin, 2005).
[33] C. Wei, S. A. Holmstrom, N. B. Manson, J. P. D. Martin, X. F. He, and P. T. H. Fisk, Appl. Magn. Reson. **11**, 521 (1996).
[34] T. Blasberg and D. Suter, Opt. Commun. **109**, 133 (1994).
[35] T. Blasberg and D. Suter, Phys. Rev. B **51**, 6309 (1995).
[36] A. Walther, A. N. Nilsson, Q. Li, L. Rippe, and S. Kröll, Eur. Phys. J. D **70**, 166 (2016).
[37] D. Serrano, J. Karlsson, A. Fossati, A. Ferrier, and P. Goldner, Nat. Commun. **9**, 2127 (2018).
[38] G. F. Koster, J. O. Dimmock, R. G. Wheeler, and H. Statz, *Properties of the Thirty-two Point Groups* (MIT Press, Cambridge, MA, 1963).
[39] B. Di Bartolo, *Optical Interactions in Solids* (Wiley, New York, 1968).
[40] B. Henderson and G. Imbush, *Optical Spectroscopy of Inorganic Solids* (Oxford University Press, New York, 2006).
[41] H.-S. Shi, G. Zhang, and H.-Y. Shen, J. Synth. Cryst. **30**, 85 (2001).
[42] E. M. Purcell, Phys. Rev. **69**, 681 (1946).
[43] D. S. Sumida and T. Y. Fan, Opt. Lett. **19**, 1343 (1994).

[44] V. E. Kisel, S. E. Troshin, N. S. Tolstik, V. G. Shcherbitsky, N. V. Kuleshov, V. N. Matrosov, T. S. Matrosova, and M. I. Kupchenko, Opt. Lett. **29**, 2491 (2004).
[45] T. Böttger, C. W. Thiel, Y. Sun, and R. L. Cone, Phys. Rev. B **73**, 075101 (2006).
[46] W. Mims, Phys. Rev. **168**, 370 (1968).
[47] Y. Sun, C. W. Thiel, R. L. Cone, R. W. Equall, and R. L. Hutcheson, J. Lumin. **98**, 281 (2002).
[48] J. Ganem, Y. P. Wang, D. Boye, R. S. Meltzer, W. M. Yen, and R. M. Macfarlane, Phys. Rev. Lett. **66**, 695 (1991).
[49] J. V. Rakonjac, Y.-H. Chen, S. P. Horvath, and J. J. Longdell, arXiv:1802.03862.
[50] P. T. H. Fisk, X. F. He, K. Holliday, and N. B. Manson, J. Lumin. **45**, 26 (1990).
[51] R. M. Macfarlane and R. M. Shelby, in *Spectroscopy of Solids Containing Rare Earth Ions*, edited by A. A. Kaplyanskii and R. M. Macfarlane (Elsevier Science BV, North-Holland, New York, 1987), pp. 51–184.
[52] J. Karlsson, N. Kunkel, A. Ikesue, A. Ferrier, and P. Goldner, J. Phys.: Condens. Matter **29**, 125501 (2017).
[53] R. L. Ahlefeldt, M. R. Hush, and M. J. Sellars, Phys. Rev. Lett. **117**, 250504 (2016).
[54] T. Zhong, J. M. Kindem, E. Miyazono, and A. Faraon, Nat. Commun. **6**, 8206 (2015).
[55] J. G. Bartholomew, R. L. Ahlefeldt, and M. J. Sellars, Phys. Rev. B **93**, 014401 (2016).
[56] R. J. Elliott and K. W. H. Stevens, Proc. R. Soc. London A **218**, 553 (1953).